AIAA JOURNAL
Vol. 42, No. 9, September 2004

Overset Field-Panel Method for Unsteady Transonic Aerodynamic Influence Coefficient Matrix Generation

P. C. Chen,* X. W. Gao,† and L. Tang†
ZONA Technology, Scottsdale, Arizona 85251

The overset field-panel method presented solves the integral equation of the time-linearized transonic small disturbance equation by an overset field-panel scheme for rapid transonic aeroelastic applications of complex configurations. A block-tridiagonal approximation technique is developed to greatly improve the computational efficiency to solve the large size volume-cell influence coefficient matrix. Using the high-fidelity computational-fluid-dynamics solution as the steady background flow, the present method shows that simple theories based on the small disturbance approach can yield accurate unsteady transonic flow predictions. The aerodynamic influence coefficient matrix generated by the present method can be repeatedly used in a structural design loop, rendering the present method as an ideal tool for multidisciplinary optimization.

Introduction

THE unsteady panel methods such as the doublet-lattice method[1] (DLM), ZONA6[2] for subsonic unsteady aerodynamics, and ZONA7[3] for supersonic unsteady aerodynamics have been well accepted by the aerospace industry for many years as the primary tools for routine aeroelastic applications. The unsteady panel methods can handle complex configurations without an extensive model-generation effort, provide expedient and accurate unsteady aerodynamic predictions, and, most important, generate the aerodynamic influence coefficient (AIC) matrices that directly relate the downwash to the unsteady pressure coefficients, that is,

$$\{\Delta C_p\} = [AIC]\{W\} \tag{1}$$

where ΔC_p is the unsteady pressure jumps and W is the downwash caused by the structural oscillations. The AIC matrix is considered as one of the key elements in the industrial aeroelastic design process because it is independent of the structural characteristics; therefore, it needs to be computed only once and repeatedly used in a structural design loop.

However, it is generally believed that the unsteady panel methods are not applicable in the transonic region because of the lack of the transonic shock effects. On the other hand, the computational-fluid-dynamic (CFD) methodology provides accurate transonic solutions by solving the Euler's or Navier–Stokes' equations, but it does not generate the AIC matrix and cannot be effectively used for routine aeroelastic applications nor for an extensive structural design/optimization. Therefore, there is a great demand from the aerospace industry to have an unsteady transonic aerodynamic method with an AIC matrix generation capability. In fact, such an unsteady transonic aerodynamic method can be developed using the unsteady field-panel method.

Integral Equations of the Unsteady Field-Panel Methods

Over the past two decades, great progress has been made in the development of the field-panel method for unsteady transonic flow computations. In 1985, Voss[4] proposed an AIC-based unsteady field-panel method using a velocity potential approach. Later, this method was improved by Lu and Voss[5] using a transonic doublet-lattice method (TDLM) to eliminate the wake modeling in the velocity potential approach. The TDLM solves the so-called time-linearized transonic small disturbance (TLTSD) equation that reads

$$\phi_{xx} + \phi_{yy} + \phi_{zz} - 2\frac{ikM_\infty^2}{\beta^2}\phi_x + \frac{k^2M_\infty^2}{\beta^2}\phi = \frac{\partial}{\partial x}(\sigma_v) \tag{2}$$

where ϕ is the perturbed unsteady velocity potential, k is the reduced frequency, M_∞ is the freestream Mach number, $\beta = \sqrt{(1 - M_\infty^2)}$, $\sigma_v = K\phi_{ox}\phi_x$. $K = (\gamma + 1)M_\infty^2/\beta^2$, and γ is the specific heat ratio.

Equation (2) is obtained by linearizing the nonlinear transonic small disturbance equation with respect to the structural oscillating amplitude, which is assumed to be small. The term ϕ_{ox} on the right-hand side (RHS) of Eq. (2) is the steady perturbation velocity component along the freestream direction, defined here as the steady background flow, which contains the steady nonlinear transonic shock effects in transonic flows. This is to say that the solution of Eq. (2) is linearly varying with the structural oscillating amplitude, but it contains the nonlinear transonic shock effects embedded in the steady background flow. Equation (2) can lead to an AIC matrix because of its linear characteristics with respect to the structural oscillating amplitude, that is, the downwash in the RHS of Eq. (1).

Assuming $(\partial/\partial x)(\sigma_v)$ on the RHS of Eq. (2) to be a volume source, the integral solution of the TLTSD equation at a point (x_0, y_0, z_0) shown in Fig. 1 consists of three parts:

$$\phi(x_0, y_0, z_0) = \phi_s + \phi_v + \phi_{\text{shock}} \tag{3}$$

In Eq. (3), ϕ_s represents the influence of the velocity potential from the surface singularities, which can be written as

$$\phi_s = \frac{1}{4\pi}\iint_s \left(\frac{\Delta C_p}{2}\bar{K} - \frac{\partial\phi}{\partial n}G\right)\mathrm{d}s \tag{4}$$

where ΔC_p and $\partial\phi/\partial n$ are the unsteady pressure jump and unsteady source distributed on the lifting surfaces and bodies, respectively. $\bar{K}$ is the acceleration potential kernel, whose detailed expression can be found in Ref. 2,

$$G = (1/R)e^{(ikM_\infty^2/\beta^2)\xi}e^{-(ikM_\infty/\beta^2)R}$$

is the unsteady source kernel and $R = \sqrt{(\xi^2 + \eta^2 + \zeta^2)}$, $\xi = x_0 - x$, $\eta = y_0 - y$, and $\zeta = z_0 - z$.

In fact, Eq. (4) is the integral solution of the linear unsteady potential equation and is the equation solved by ZONA6 for the

Received 5 August 2003; revision received 22 January 2004; accepted for publication 17 April 2004.

*Vice President, 7430 E. Stetson Drive, Suite 205; www.zonatech.com. Member AIAA.
†Engineering Specialist, 7430 E. Stetson Drive, Suite 205.

wing-body configurations. The TDLM is formulated for the lifting surface only, that is, the unsteady source integral for bodies is absent. Here, we adopt the ZONA6 formulation to handle complex configurations such as the wing-body combinations. In the ZONA6 paneling scheme, the configuration surfaces are descritized into many small boxes, called the surface boxes, leading to a matrix that relates the surface singularity strength to the normal velocity on each box.

The second and third terms on the RHS of Eq. (3) read

$$\phi_v = -\frac{1}{4\pi}\iiint_V \frac{\partial}{\partial x}(\sigma_v) G \, \mathrm{d}V \tag{5}$$

$$\phi_{\text{shock}} = \frac{1}{4\pi}\iint_{\text{shock}} \Delta\sigma_v G \, \mathrm{d}S \tag{6}$$

In Eq. (5) and (6), ϕ_v is the influence of the velocity potential from the volume source, and ϕ_{shock} is the influence of the velocity potential from the shock surface on which $\Delta\sigma_v$ represents the jump of the volume source strength across the shock surface. Note that ϕ_{shock} automatically vanishes if the transonic shock is absent because $\Delta\sigma_v = 0$. In addition, in the presence of shock, ϕ_{shock} can be eliminated by performing integration by parts for the volume integral of ϕ_v such that

$$\phi_v = -\lim_{\varepsilon \to 0} \frac{1}{4\pi}\iint_{yz} \left\{ \int_{-\infty}^{x_s - \varepsilon} + \int_{x_s - \varepsilon}^{x_s + \varepsilon} + \int_{x_s + \varepsilon}^{\infty} \right\} \times \frac{\partial}{\partial x}(\sigma_v) G \, \mathrm{d}x \, \mathrm{d}y \, \mathrm{d}z \tag{7}$$

gives

$$\phi_v = -\lim_{\varepsilon \to 0} \frac{1}{4\pi}\iint_{yz} \sigma_v G \Big|_{x_s - \varepsilon}^{x_s + \varepsilon} \mathrm{d}S + \frac{1}{4\pi}\iiint_V \sigma_v G_x \, \mathrm{d}V \tag{8}$$

where x_s represents the shock location and ε represents an infinitesimal thickness of the shock surface.

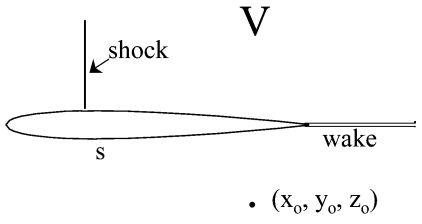

Fig. 1 Integration domain of the integral solution.

Combining Eqs. (8) and (6) yields

$$\phi_{\text{shock}} + \phi_v = \frac{1}{4\pi}\iiint_V \sigma_v G_x \, \mathrm{d}V \tag{9}$$

A similar derivation from Eqs. (2–9) but for the time domain small disturbance equation can be found in Ref. 6. In addition, the theoretical foundation of the field-panel method using the Green's function method has been well established by Ref. 6.

Equation (9) can be recast into a matrix equation by first defining a volume block surrounding the lifting surfaces or bodies and then descritizing the volume block into many small volume cells. A typical volume-cell modeling for lifting surfaces and bodies is shown in Fig. 2.

Unlike the CFD methodology whose volume mesh must be extended far away from the surface mesh, the domain of the volume block for the field-panel method needs only to contain the nonlinear flow region in which the volume source strength σ_v is significant. This is because outside the domain of the volume block the solution is dominated by Eq. (4); thereby the contribution from Eq. (9) can be ignored.

At a point located on the surface boxes, the normal perturbation velocity reads

$$\{\boldsymbol{n} \cdot \boldsymbol{\nabla}\phi\} = \{W\} = [A] \begin{Bmatrix} \Delta C_p \\ \dfrac{\partial \phi}{\partial n} \end{Bmatrix} + [B]\{\sigma_v\} \tag{10}$$

At a point located in the volume cells, the velocity potential reads

$$\{\phi\} = [C] \begin{Bmatrix} \Delta C_p \\ \dfrac{\partial \phi}{\partial n} \end{Bmatrix} + [D]\{\sigma_v\} \tag{11}$$

where $\boldsymbol{n} \cdot \boldsymbol{\nabla}\phi$ represents the normal perturbation velocity on the surface boxes; matrices $[A]$ and $[C]$ contain the influence coefficients from the surface singularities to the points on the surface boxes and in the volume cells, respectively; and matrices $[B]$ and $[D]$ contain the influence coefficients from the volume sources to the points on the surface boxes and in the volume cells, respectively.

Equation (10) can be linked to Eq. (11) by relating σ_v to ϕ through a finite difference operator $[T]$ such that

$$\{\sigma_v\} = [T]\{\phi\} \tag{12}$$

Voss[4] suggested that such a finite difference operator can be formulated using the Murman's scheme,[7] which reads

$$\sigma_v = (1 - \mu_i)\sigma_{vi} + \mu_{i-1}\sigma_{vi-1} + \mu_i \phi_{xi} - \mu_{i-1}\phi_{xi-1} \tag{13}$$

where $\mu_i = 0$ for $M_i < 1$ and $\mu_i = 1$ for $M_i \geq 1$, M_i is the local Mach number in the ith volume cell, and i is the index of the volume cells along the freestream direction.

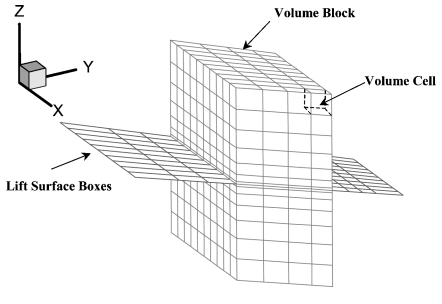

a) Lifting surfaces

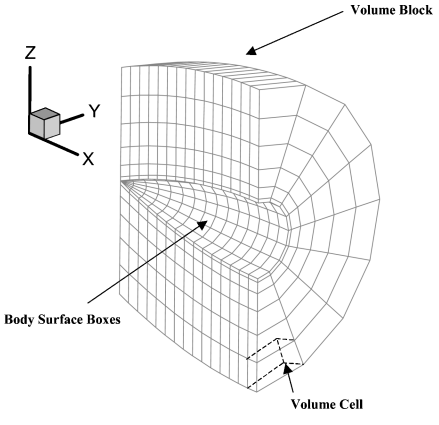

b) Bodies

Fig. 2 Typical volume-cell modeling for lifting surfaces and bodies.

Murman's scheme is a conservative finite difference operator and guarantees the correct mathematical shock jumps. It automatically switches from the central differencing in the subsonic flows to the backward differencing in the supersonic flows, and thereby introduces the directional bias to the integral equations of TLTSD for handling the mixed flow problems of the transonic flow. The detailed expression of the matrix $[T]$ using the Murman's scheme can be found in Ref. 8.

Substituting Eq. (12) into Eq. (10) and (11) and combining the resulting equations yields

$$\{W\} = [\bar{A}] \begin{Bmatrix} \Delta C_p \\ \dfrac{\partial \phi}{\partial n} \end{Bmatrix} \tag{14}$$

where

$$[\bar{A}] = [A] + [B][T][E]^{-1}[C] \tag{15}$$

$$[E] = [I] - [D][T] \tag{16}$$

Inverting the matrix $[\bar{A}]$ gives the AIC matrix such as the one shown in Eq. (1). Note that the size of the AIC matrix is only the number of surface boxes, and the form of the AIC matrix is identical to that of the DLM, ZONA6, and ZONA7. This is a very attractive feature for industrial aeroelastic applications because once the AIC matrix is obtained all downstream AIC-based aeroelastic solution procedures for flutter, aeroservoelastic, and dynamic loads analyses remain unchanged.

However, the unsteady field-panel method does have several technical issues that need to be resolved before it can be adopted as an industrial tool for expedient unsteady aerodynamic computations.

Block-Tridiagonal Approximation of the $[E]$ Matrix

The matrix $[E]$ in Eq. (16) is a complex and fully populated matrix whose size is the number of volume cells. To model a general three-dimensional problem might require more than 10,000 volume cells, and this number increases rapidly as the complexity of the configurations increases. Therefore, to invert (or decompose) such a large matrix is impractical for routine aeroelastic applications. In the present method, a block-tridiagonal approximation technique is employed to circumvent this technical issue.

The idea behind the block-tridiagonal approximation technique is a simple one. First, the volume cells are grouped into many subblocks. For instance, the volume blocks on the top and bottom of the lifting surface can be divided into several subblocks, and the volume cells within the same subblock are grouped together. In so doing, the matrix $[E]$ can be written as

$$[E] = [E_B] + [E_\varepsilon] \tag{17}$$

where $[E_B]$ is a block-tridiagonal matrix whose tridiagonal blocks contain the influence coefficients from the self-block and the adjacent sub-blocks. $[E_\varepsilon]$ contains zeros in the tridiagonal blocks and the influence coefficients from the nonadjacent blocks in the off-tridiagonal blocks.

Next, by comparing the order of magnitude of the coefficients in the matrix $[E_\varepsilon]$ to the matrix $[E_B]$, it can be seen that all coefficients of $[E_\varepsilon]$ are small. This is because the integrand in the integral equation shown in Eq. (5) contains an $1/R$ function that decays rapidly when the point (x_0, y_0, z_0) is away from the nonadjacent subblocks. Therefore, the inverse of the matrix $[E]$ can be solved approximately by the following equation:

$$[E]^{-1} \approx [E_B]^{-1} - [E_B]^{-1}[E_\varepsilon][E_B]^{-1} \tag{18}$$

Finally, because $[E_B]$ is block-tridiagonal, $[E_B]^{-1}$ can be computed efficiently using a block-tridiagonal matrix solver. In addition, because the block-tridiagonal matrix solver only needs to hold three block matrices in the computer memory at a time, a large amount of computer memory for solving $[E]^{-1}$ can be saved.

Overset Field-Panel Scheme for Complex Configurations

The objective of the overset field-panel scheme is to minimize the volume-cell generation effort for complex configurations. For a simple lifting surface or body shown in Fig. 2, the generation of volume cells can be automated by simply specifying the height and number of layers of the volume block. However, to generate a set of conformal volume cells over a complex configuration such as a wing with underwing stores requires an extensive volume-cell generation (or grid generation) effort.

The overset field-panel scheme allows the volume cells to be generated independently on each component of the complex configuration. For instance, a wing with an underwing missile, a pylon, and fins shown in Fig. 3 can be separated into multiple components: wing, pylon, missile body, and fins. On each component, a volume block is defined independently, which can be automatically divided into volume cells. Therefore, among all volume blocks volume cells of different volume blocks can intersect each other. The overset field-panel scheme constructs the influence coefficient matrices of such an overset volume-cell model based on the following procedure:

1) Volume cells in different volume blocks do not influence each other.

2) Volume cells in the same volume block influence only their associated surface boxes.

3) All surface boxes influence all volume cells.

The preceding overset field-panel scheme is formulated with the realization that the interference between volume blocks can be transmitted through the integral equations shown in Eq. (3). Unlike the overset CFD methodology where the interpolation of the flow solutions in the overset region is required, the overset field-panel scheme

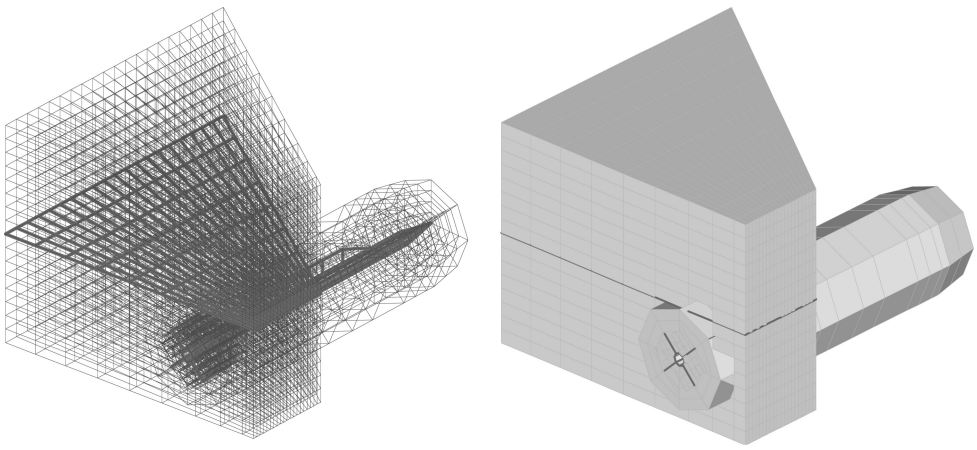

Fig. 3 Overset field-panel scheme for a wing with an underwing missile.

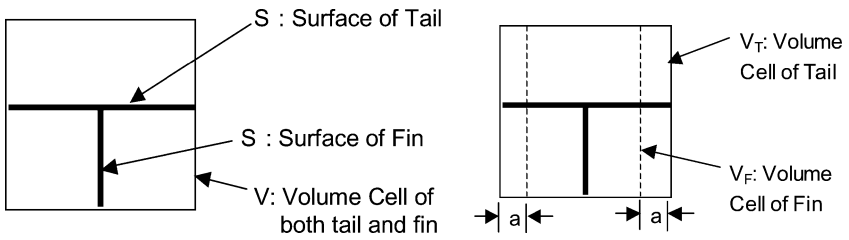

a) One-block modeling **b) Overset modeling**

Fig. 4 One-block modeling and overset modeling of a T-tail configuration.

does not need such an interpolation. Therefore there is no need to compute the topology of the intersection among cells, greatly simplifying the volume-cell generation effort for complex configurations. To verify this scheme, let us consider a T-tail configuration consisting of a horizontal tail and a vertical fin. This T-tail configuration can be modeled by a single rectangular volume block whose volume cells are conformed to the surfaces of the tail and the fin. This one-block modeling is shown in Fig. 4a, and its influence coefficient matrix equations read

$$\begin{Bmatrix} W_{S_T} \\ W_{S_F} \end{Bmatrix} = [A] \begin{Bmatrix} \Delta C_{p_{S_T}} \\ \Delta C_{p_{S_F}} \end{Bmatrix} + \left[B_{\mathrm{VS}_T}, B_{\mathrm{VS}_F} \right] \{(\sigma_v)_v\}$$

$$\{\phi_v\} = \left[C_{S_T V}, C_{S_F V} \right] \begin{Bmatrix} \Delta C_{p_{S_T}} \\ \Delta C_{p_{S_F}} \end{Bmatrix} + [D_{\mathrm{VV}}] \{(\sigma_v)_v\} \qquad (19)$$

where the subscripts S_T and S_F denote the surface boxes of the tail and of the fin, respectively. The subscript V denotes the volume cells of the one-volume block, $(\,)_{\mathrm{VS}_T}$ is the influence from V to S_T, $(\,)_{\mathrm{VS}_F}$ is the influence from V to S_F, $(\,)_{S_T V}$ is the influence from S_T to V, $(\,)_{S_F V}$ is the influence from S_F to V, and $(\,)_{\mathrm{VV}}$ is the influence from V to V.

Equation (19) can be considered as "exact" because of the one-block modeling. The same T-tail configuration can be also modeled by two volume blocks, one for the tail and one for the fin, which are depicted by the solid box and the dashed box in Fig. 4b, respectively. Figure 4b also shows that the width of the volume block of the fin is shorter than that of the tail by 2a. Apparently, the volume cells of the fin are all embedded in those of the tail, rendering an overset field-panel model. The influence coefficient matrix equations of this overset field-panel model can be written as

$$\begin{Bmatrix} W_{S_T} \\ W_{S_F} \end{Bmatrix} = [A] \begin{Bmatrix} \Delta C_{p_{S_T}} \\ \Delta C_{p_{S_F}} \end{Bmatrix} + \begin{bmatrix} B_{v_T S_T} & 0 \\ 0 & B_{v_F S_F} \end{bmatrix} \begin{Bmatrix} (\sigma_v)_{v_T} \\ (\sigma_v)_{v_F} \end{Bmatrix}$$

$$\begin{Bmatrix} \phi_{v_T} \\ \phi_{v_T} \end{Bmatrix} = \begin{bmatrix} C_{S_T v_T} & C_{S_F v_T} \\ C_{S_T v_F} & C_{S_F v_F} \end{bmatrix} \begin{Bmatrix} \Delta C_{p_{S_T}} \\ \Delta C_{p_{S_F}} \end{Bmatrix} + \begin{bmatrix} D_{v_T v_T} & 0 \\ 0 & D_{v_F v_F} \end{bmatrix} \begin{Bmatrix} (\sigma_v)_{v_T} \\ (\sigma_v)_{v_F} \end{Bmatrix} \qquad (20)$$

where the subscripts V_T and V_F denote the volume cells of the tail and fin, respectively.

When $a = 0$, because the domain of the tail volume block is identical to that of the fin, it is obvious that $C_{S_T V_F} = C_{S_T V_T} = C_{S_T V}$, $C_{S_F V_T} = C_{S_F V_F} = C_{S_F V}$, $B_{V_T S_T} = B_{\mathrm{VS}_T} = B_{V_F S_F} = B_{\mathrm{VS}_F}$ and $D_{V_T S_T} = D_{V_F S_F} = D_{\mathrm{VV}}$; therefore, $\phi_{V_T} = \phi_{V_F} = \phi_V$ and $(\sigma_v)_{v_T} = (\sigma_v)_{v_F} = (\sigma_v)_v$. Thus, the solution of the one-block modeling and the overset field-panel model is identical if $a = 0$.

When $a \neq 0$, the overset field-panel modeling becomes an approximation of the one-block modeling. However, because the domain of a is far away from the fin, its contribution of the influence to the fin is small and can be ignored as long as a is not very large.

The overset field-panel scheme can also greatly reduce the computer memory and CPU time for solving the $[E]$ matrix. As shown in Eq. (20), because the volume cells in different volume blocks do not influence each other, the $[D]$ matrix becomes block diagonal, leading to a block-diagonal $[E]$ matrix that can be inverted based on a block-by-block procedure. Furthermore, the block-tridiagonal approximation technique can be applied to invert each diagonal block matrix to further increase the computational efficiency.

Steady Background Flow from the High-Fidelity CFD Codes

It is well known that the transonic small disturbance theory might not provide accurate solutions for strong transonic shock cases because it cannot correctly model the entropy gradients from strong shock nor convect the vorticity. However, this is not to say that the transonic small disturbance theory is not suitable for the prediction of unsteady flows because of small aeroelastic deformations if the total unsteady flow is decomposed into a steady background flow and an unsteady of small disturbances. As demonstrated by Liu et al.,[9] simplified theories based on the small disturbance approach can yield accurate unsteady flow predictions provided that the steady background flow on which the unsteady disturbance propagate is accurately accounted for. This suggests that, if the steady background flow in the TLTSD equation is externally provided by a high-fidelity CFD steady solution, accurate unsteady flow predictions can be ensured. This is also evident by examining the Murman's scheme shown in Eq. (13), where the switching scheme from the central differencing to the backward differencing is based on the local Mach numbers of the steady background flow. Thus, the unsteady shock location is dominated by the steady shock location in the small amplitude sense, implying that accurate steady shock structures can ensure the accuracy of the unsteady shock structures.

To date, many high-fidelity CFD codes for the accurate prediction of steady flow over realistic aircraft configurations for transonic flight conditions are available. Thus, the steady background flow of the present method can be directly imported from these CFD codes. In addition, because the CFD mesh is usually much more refined than the volume cells of the field-panel method, to import the CFD steady flow solutions can be easily achieved by a simple interpolation of the CFD steady solution from the CFD mesh to the volume cells.

Validation of the Unsteady Pressure Distribution

Four test cases are selected to validate the unsteady pressure coefficients with the experimental data. The steady background flow of all four test cases are computed by the CFL3D Navier–Stokes solver[10] and interpolated to the volume cells.

F-5 Wing Pitching About 50% Root Chord at $M_\infty = 0.9$ and $k = 0.275$

Figure 5 depicts the field-panel model and the CFL3D surface mesh of an F-5 wing. The field-panel model consists of 20×10 surface boxes and $25 \times 12 \times 12$ volume cells, whereas the CFL3D mesh contains $181 \times 77 \times 71$ grid points for the Navier–Stokes computation. The CFL3D steady pressure coefficients Cp at $M_\infty = 0.9$ and angle of attack $= 0$ deg ($\alpha = 0$ deg) are first compared to the wind-tunnel measurements[11] and are shown in Fig. 6 for three span stations at $y/2b = 51.5$, 87.5, and $= 97.7\%$. Excellent agreement is obtained except at $y/2b = 97.7\%$, where CFL3D slightly underpredicts the shock strength on the upper surface.

Using the CFL3D solution as the steady background flow, the unsteady ΔCp along the same three span stations computed by the present method at $M_\infty = 0.9$ and $k = 0.275$ caused by a pitch oscillation about the 50% root chord is shown in Fig. 7. By comparing the

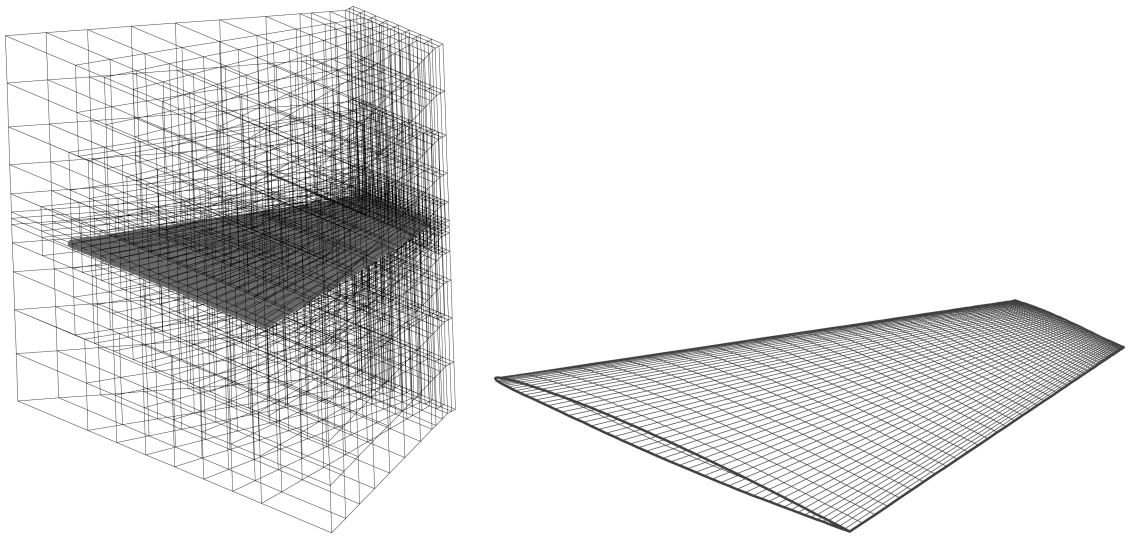

a) Field-panel method b) CFL3D surface mesh

Fig. 5 Field-panel model and CFL3D surface mesh of a F-5 wing.

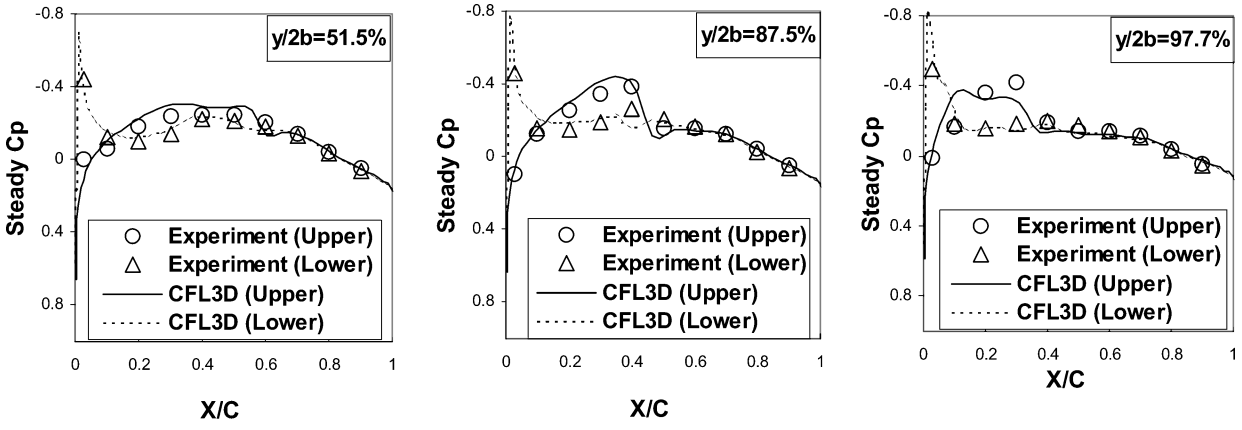

Fig. 6 Comparison of steady *Cp* between CFL3D and wind-tunnel results on a F-5 wing at $M_\infty = 0.9$, $\alpha = 0$ deg, and $Re = 9 \times 10^5$.

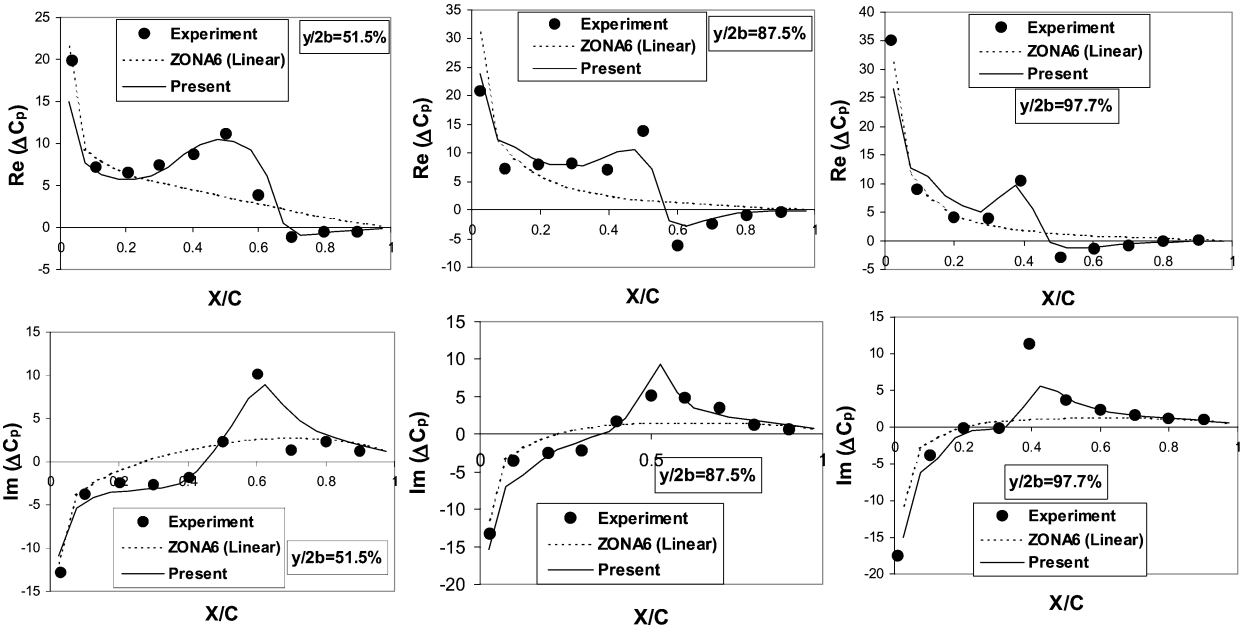

Fig. 7 Unsteady ΔCp on a F-5 wing caused by a pitch oscillation about 50% chord at $M_\infty = 0.9$ and $k = 0.275$.

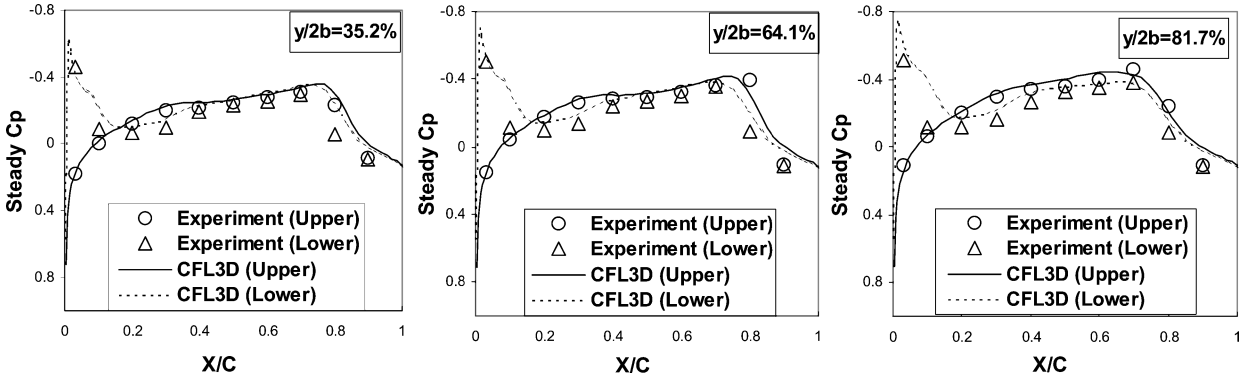

Fig. 8 Comparison of steady *Cp* between the CFL3D and wind-tunnel results on a F-5 wing at $M_\infty = 0.948$, $\alpha = -0.006$ deg, and $Re = 9 \times 10^5$.

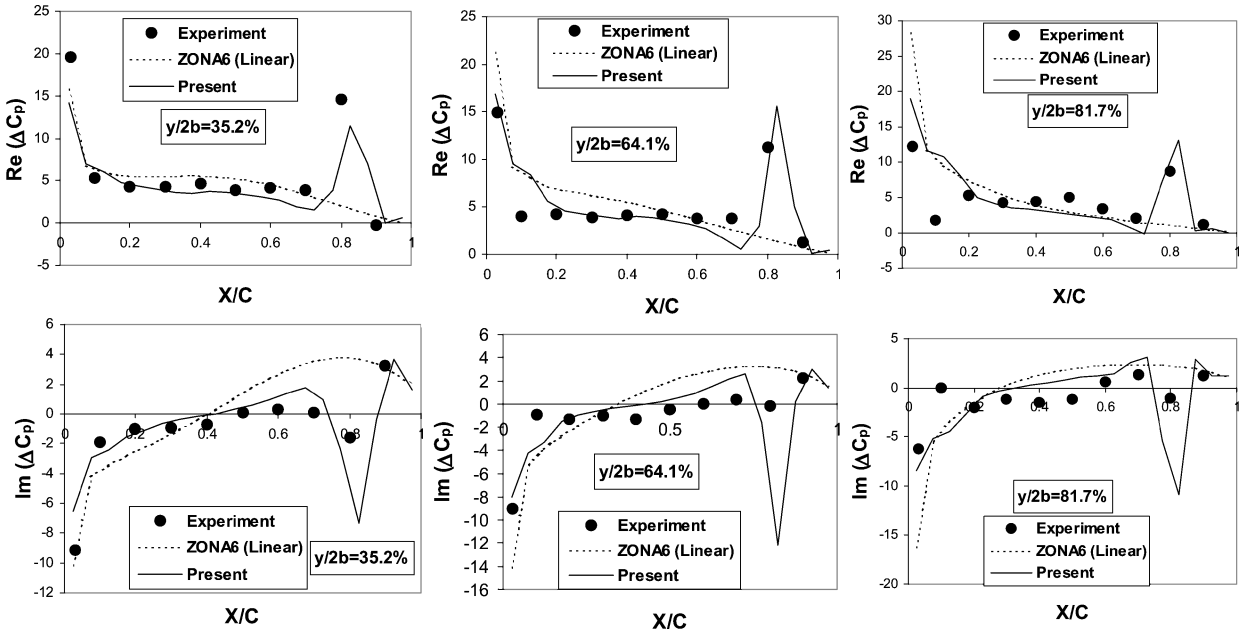

Fig. 9 Unsteady *Cp* on a F-5 wing caused by pitch oscillations about 50% root chord at $M_\infty = 0.948$ and $k = 0.264$.

present method to the wind-tunnel measurements, it can be seen that a good correlation is obtained except at $y/2b = 97.7\%$, where the present method underpredicts the unsteady shock strength. This is probably caused by the underprediction of the CFL3D steady shock strength $y/2b = 97.7\%$. Also shown in Fig. 7 by the dashed line is the linear results computed by ZONA6, which fails to predict the unsteady shock effects, as expected.

F-5 Wing Pitching About 50% Root Chord at $M_\infty = 0.948$ and $k = 0.264$

The same field-panel model and CFL3D mesh shown in Fig. 5 are employed for this case. The comparison of steady Cp at $M_\infty = 0.948$ and $\alpha = -0.006$ deg between the CFL3D and wind-tunnel results is presented in Fig. 8 for three span stations: $y/2b = 35.2$, 64.1, and 81.7%.

Compared to the steady Cp at $M_\infty = 0.9$, the steady transonic shocks at $M_\infty = 0.948$ become stronger and move toward the trailing edge. For this strong shock case, CFL3D captures the steady shock location well but slightly overpredicts the shock strength on the lower surface at all three span stations. Therefore, overprediction of the unsteady shock strength by the present method is expected.

Indeed, in Fig. 9 the unsteady ΔCp at $M_\infty = 0.948$ and $k = 0.264$ computed by the present method shows the overprediction of the unsteady shock strength at all three span stations. However, its predicted unsteady shock locations correlate well with the wind-tunnel measurements because of the correct steady shock locations predicted by CFL3D.

Lessing Wing in First Bending Mode at $M_\infty = 0.9$ and $k = 0.13$

The Lessing wing[12] has a rectangular planform with an aspect ratio = 3.0 and a 5% parabolic arc section. Figure 10 presents the field-panel model and the CFL3D surface mesh of the Lessing wing where the field-panel model consists of 11×20 surfaces boxes and $25 \times 13 \times 12$ volume cells and the CFL3D mesh contains $181 \times 17 \times 71$ viscous grid. Shown in Fig. 11 is the comparison of steady Cp at $M_\infty = 0.9$ and $\alpha = 0.0$ deg between the CFL3D and wind-tunnel results at $y/2b = 50$, 70, and 90%. Excellent agreement is obtained by CFL3D except at $y/2b = 90\%$, where CFL3D underpredicts both the steady shock location and strength.

The magnitude and phase angle of the unsteady ΔCp on the Lessing wind as a result of the first bending mode at $M_\infty = 0.9$ and $k = 0.13$ are presented in Fig. 12, where good correlation between the present method and the wind-tunnel data can be seen except at $y/2b = 90\%$. Again, this discrepancy is probably caused by the underprediction of the steady shock location and strength at $y/2b = 90\%$ by CFL3D.

LANN Wing Pitching About 62% Root Chord at $M_\infty = 0.822$ and $k = 0.105$

As was discussed earlier, it is generally believed that the small disturbance theories cannot give accurate aerodynamic predictions on the supercritical wings in the presence of strong shock. To show that this is not the case for the unsteady flow predictions using the present method, the unsteady pressure measurement on the LANN

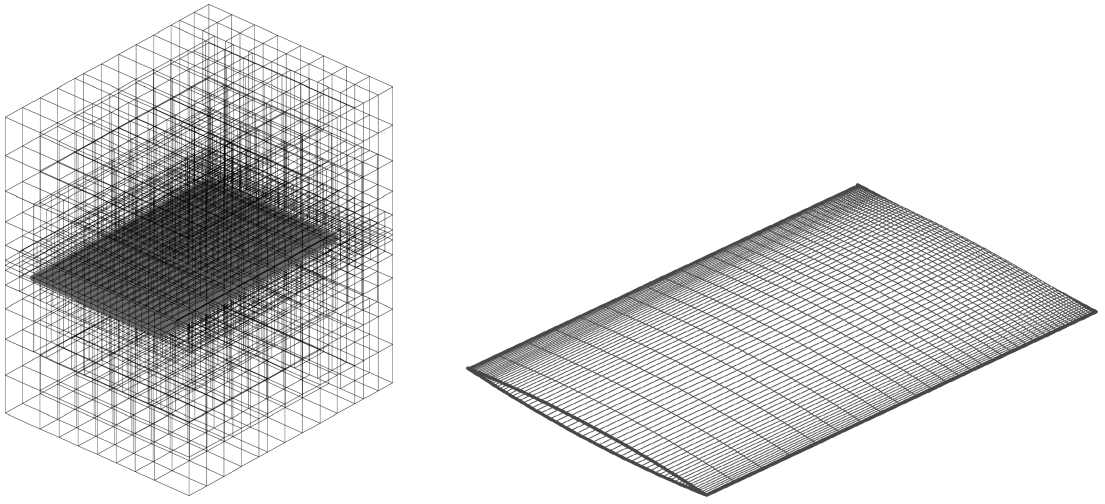

a) Field-panel model b) CFL3D surface mesh

Fig. 10 Field-panel model and CFL3D surface mesh of the Lessing wing.

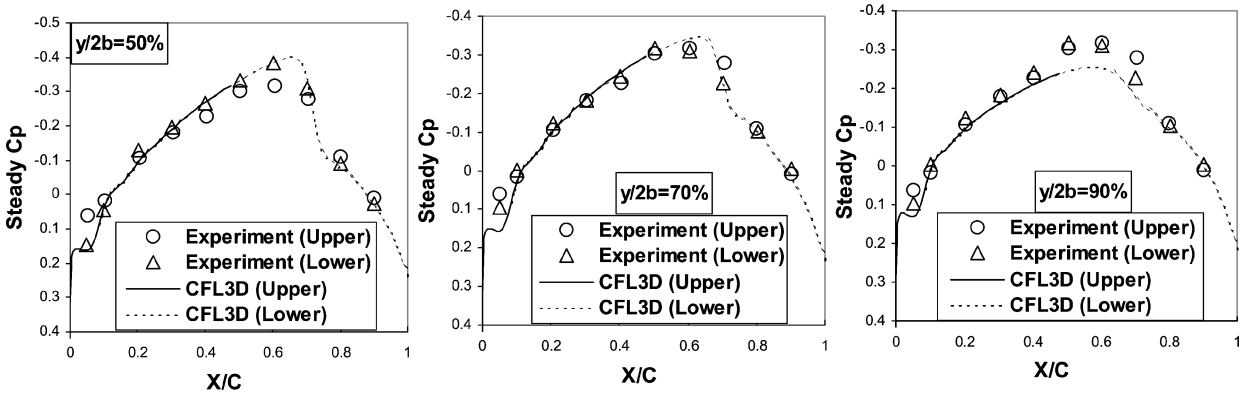

Fig. 11 Comparison of steady Cp between the CFL3D and wind-tunnel results on a Lessing wing at $M_\infty = 0.9$, $\alpha = -0.0$ deg, and $Re = 9 \times 10^5$.

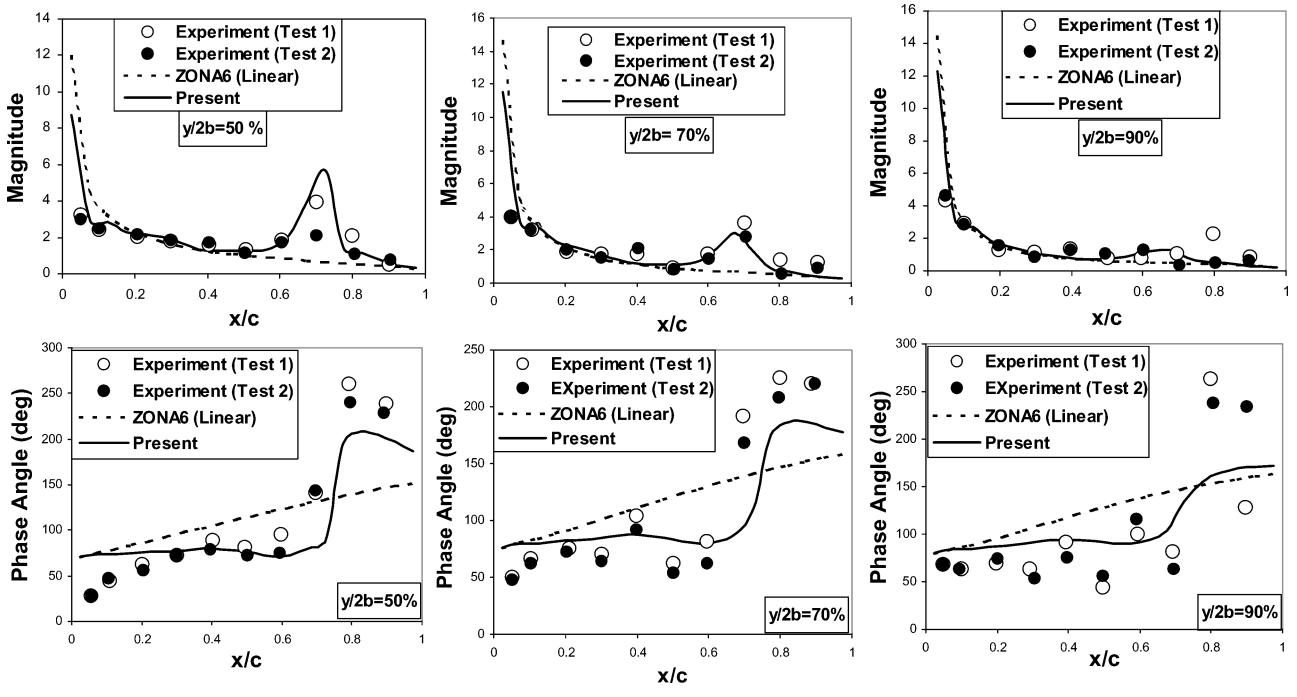

Fig. 12 Magnitude and phase angle of the unsteady ΔCp in a Lessing wing caused by the first bending mode at $M_\infty = 0.9$ and $k = 0.13$.

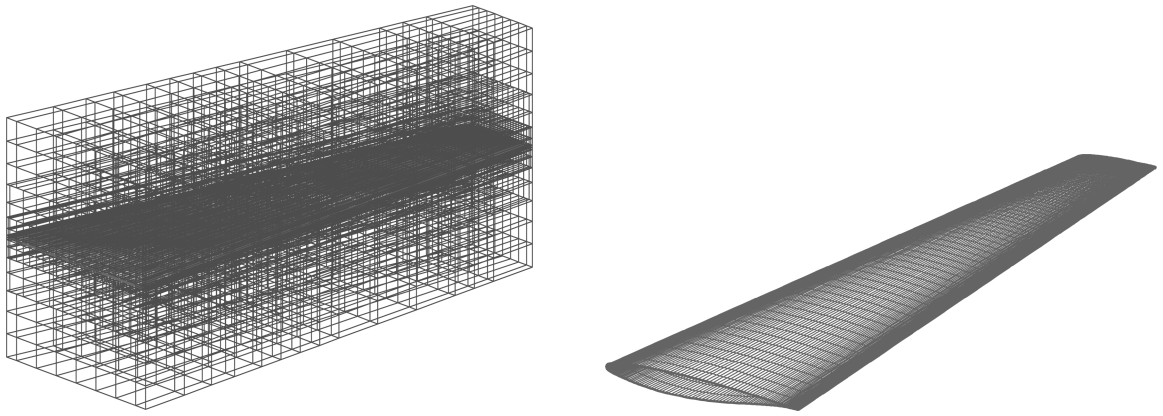

a) Field-panel model b) CFL3D surface mesh

Fig. 13 Field-panel model and CFL3D surface mesh of a LANN wing.

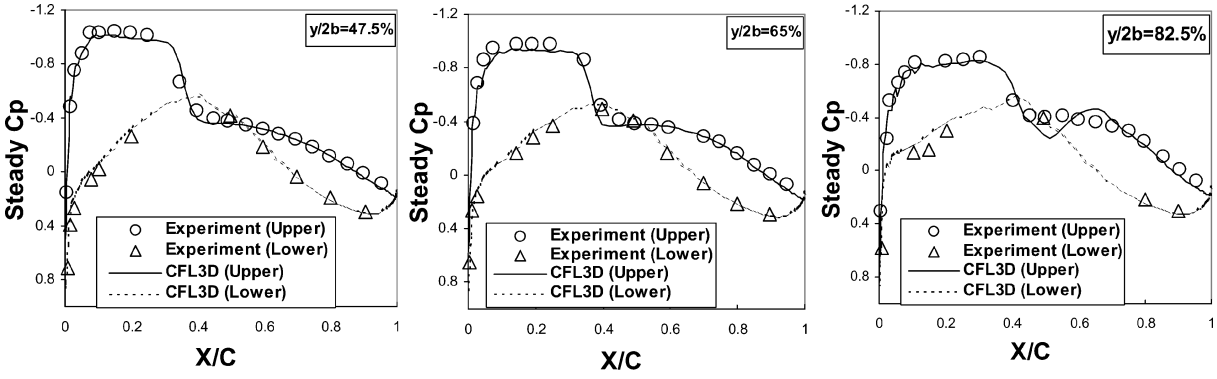

Fig. 14 Steady Cp on a LANN wing at $M_\infty = 0.822$, $\alpha = 0.6$ deg, and $Re = 4.6 \times 10^6$.

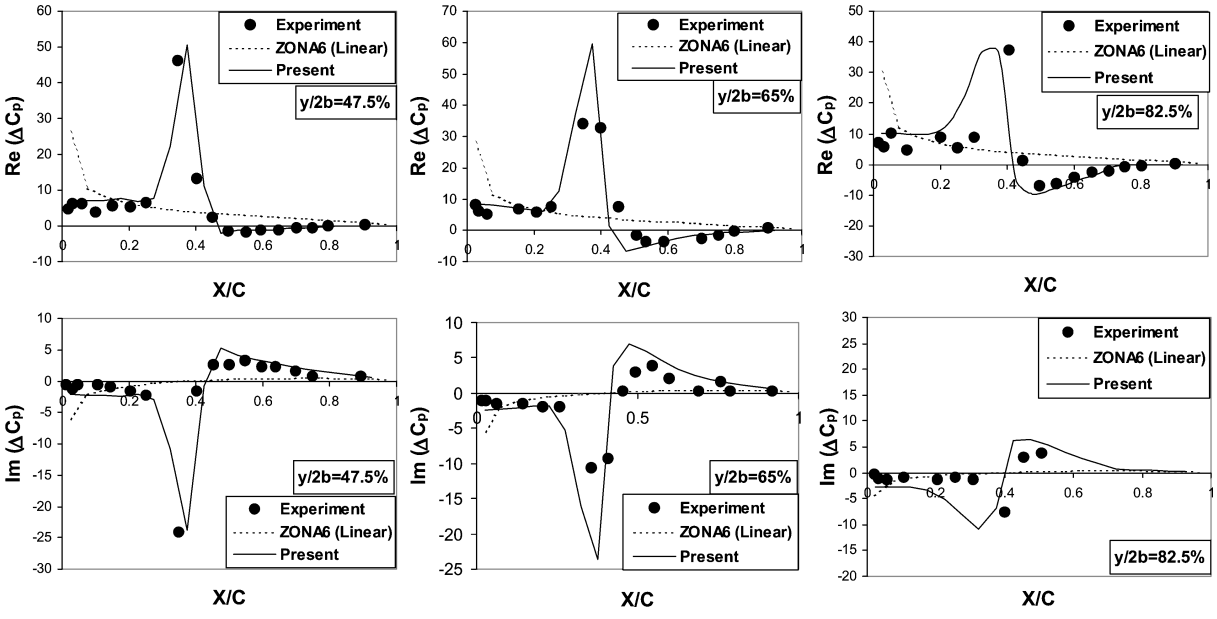

Fig. 15 Unsteady ΔCp on a LANN wing as a result of a pitch oscillation about 62% root chord at $M_\infty = 0.822$ and $k = 0.105$.

wing[13] is selected for validation. The LANN wing is a supercritical wing with an aspect ratio = 7.92 and a 25-deg swept angle along $\frac{1}{4}$-chord, whose field-panel model and the CFL3D surface mesh are depicted in Fig. 13. The field-panel model of the LANN wing consists of 20×14 surface boxes and $24 \times 16 \times 16$ volume cells, whereas the CFL3D mesh contains a $269 \times 131 \times 71$ viscous grid.

The CFL3D steady Cp at $M_\infty = 0.822$ and $\alpha = 0.6$ deg and at three span stations $y/2b = 47.5$, 65, and 82.5% are compared with the wind-tunnel measured results and are shown in Fig. 14. It can be seen that the steady shock location and strength are well captured by CFL3D except at $y/2b = 82.5\%$, where the shock location on the upper surface is slightly underpredicted.

The unsteady ΔCp obtained by the present method, wind-tunnel testing, and ZONA6 on the LANN wing caused by a pitch oscillation about 62% root chord at $M_\infty = 0.822$ and $k = 0.105$ are presented in Fig. 15. Good agreement with the wind-tunnel results at $y/2b = 47.5$ and 65% is obtained by the present method. At $y/2b = 82.5\%$ the present method underestimates the unsteady shock location, again, probably because of the underpredicted steady shock location by CFL3D. For this LANN wing case the ZONA6 results (dashed lines

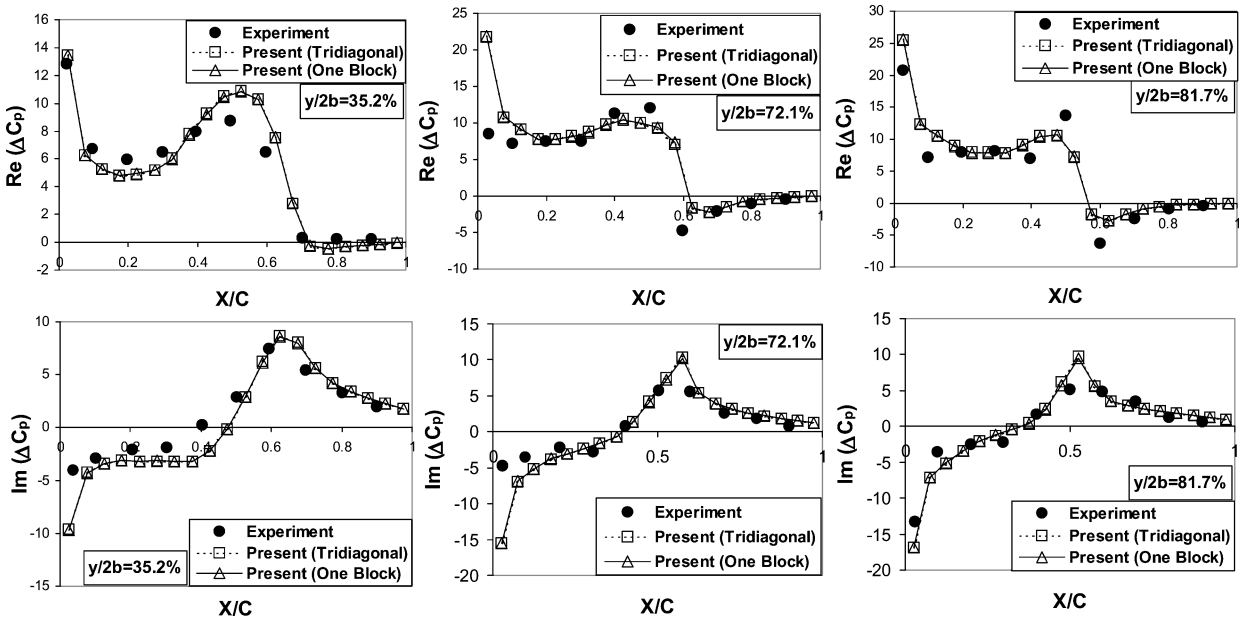

Fig. 16 Validation of the block-tridiagonal approximation technique on an F-5 wing at $M_\infty = 0.9$ and $k = 0.275$.

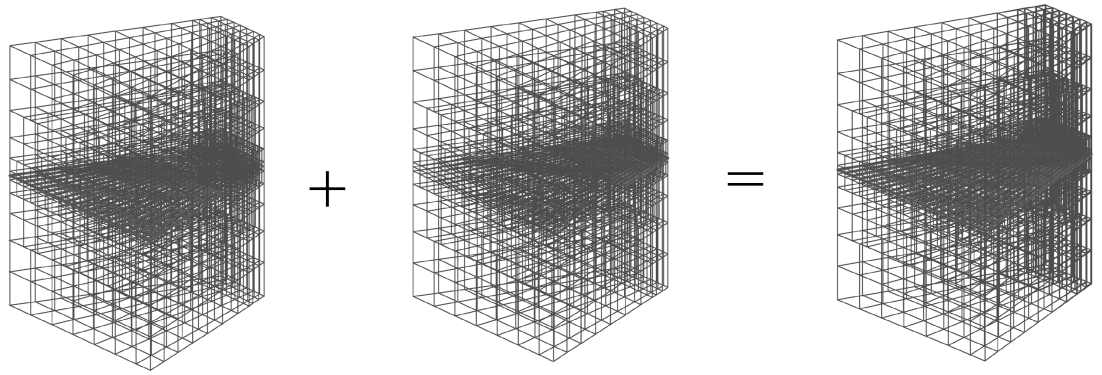

a) Root section **b) Tip section** **c) Overset field-panel model**

Fig. 17 Overset field-panel model of a F-5 wing with two volume blocks.

in Fig. 15) are totally unacceptable, indicating that the linear aerodynamic theories have little applicability to supercritical wings in transonic Mach numbers.

Validation of the Block-Tridiagonal Approximation Technique

The F-5 wing at $M_\infty = 0.9$ and $k = 0.275$ case is selected to validate the block-tridiagonal approximation technique. The one-block field-panel model shown in Fig. 5 is divided into six subblocks along the span. Because there are 12 strips of surface boxes, each subblock evenly occupies two strips of the surface boxes, rendering $25 \times 12 \times 2$ volume cells in each subblock. The result of the six-subblock model is computed using the block-tridiagonal approximation technique and compared to that of the one-block model. As seen in Fig. 16, nearly identical results between those two sets of results are obtained, showing the validity of the block- tridiagonal approximation technique. The six-subblock model gives an approximately 50% reduction in CPU time over that of the one-block model. It is believed that more significant computing time can be saved by the block-tridiagonal approximation technique for more complex configurations.

Validation of the Overset Field-Panel Scheme

The validation of the overset field-panel scheme can be performed by comparing the results between the overset modeling and the one-block modeling. Again, we select the F-5 wing at $M_\infty = 0.9$ and $k = 0.275$ as the test case where the F-5 wing is first separated into two pieces of lifting surface (denoted as the "root section" shown in Fig. 17a and the "tip section" shown in Fig. 17b) along $y/2b = 62.9\%$. Next, two volume blocks both have the full span of the F-5 wing, that is, two identical volume blocks sharing the same three-dimensional domain are defined for the root section and the tip section, respectively. Figure 17c depicts that, when joining the root section and the tip section together, an overset field-panel model of the F-5 wing is generated. According to the overset field-panel scheme, these two blocks do not influence each other, and the interference between them is through the influence from the surface boxes. Because the domain of the two volume blocks is identical, there is no approximation of the overset field-panel scheme, and an identical result between the two-block model and the one-block model is expected.

Indeed, as shown in Fig. 18, the result of the two-block overset model of the F-5 wing is nearly identical to that of the one-block model, verifying the mathematical "correctness" of the overset field-panel scheme.

Validation of Flutter Boundary Predictions

Three test cases are selected to validate the flutter boundary prediction of the present method with the wind-tunnel measurements. Again, the steady background flows of all cases are computed using the CFL3D Navier–Stokes solver.

AGARD 445.6 Wing Flutter Boundary

The AGARD 445.6 wing[14] has two types of stiffness, the weakened wing and the solid wing, and both wings have the same

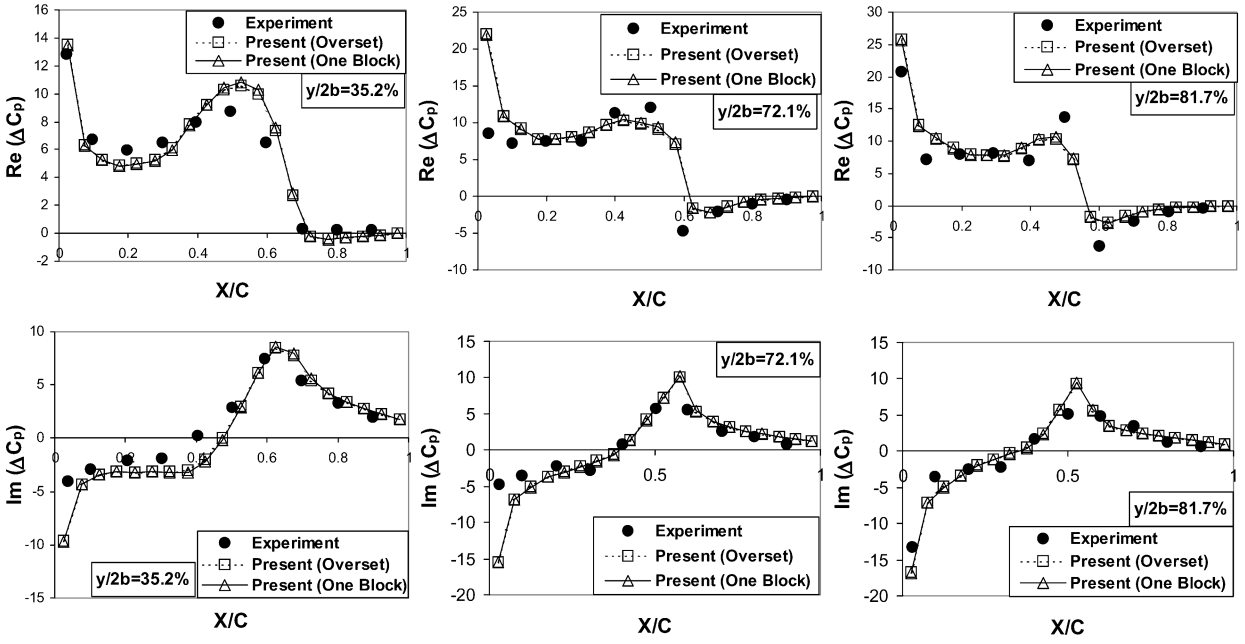

Fig. 18 Validation of the overset field-panel scheme on a F-5 wing at $M_\infty = 0.9$ and $k = 0.275$.

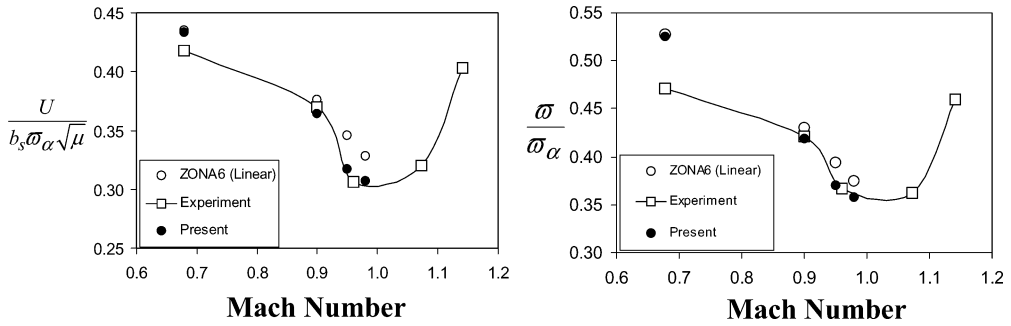

Fig. 19 Flutter boundary of the AGARD 445.6 weakened wing.

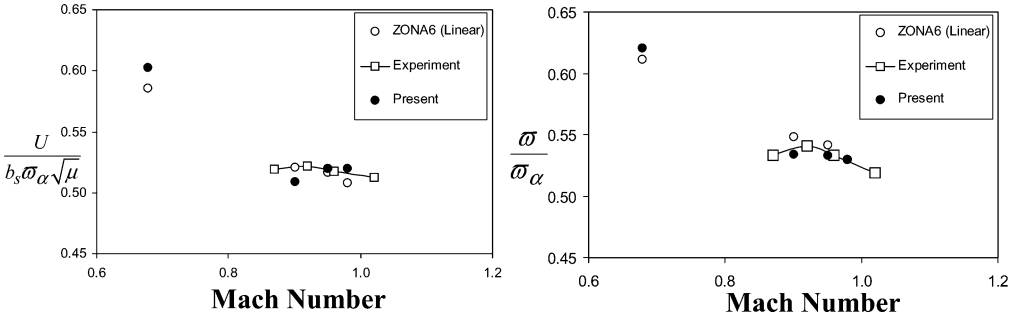

Fig. 20 Flutter boundary of the AGARD 445.6 solid wing.

aerodynamic geometry, giving an ideal case to demonstrate the AIC capability of the present method. Because the AIC matrix only depends on the aerodynamic geometry and is independent of the structural characteristics, the AIC matrix of the weakened wing can be saved and reused for the solid wing. Four AIC matrices of the weakened wing at $M_\infty = 0.678$, 0.9, 0.95, and 0.98 are first generated, and the corresponding flutter speed indexes $[(U/bs)\omega_\alpha\sqrt{\mu}]$ and flutter frequencies (ω/ω_α) are shown in Fig. 19. It can be seen that the transonic flutter dip of the weakened wing is well predicted by the present method. Meanwhile, the linear results computed by ZONA6 give large discrepancy in the transonic region, as expected.

Figure 20 presents the flutter boundary of the solid wing predicted by the present method but using the AIC matrices of the weakened wing. Again, good correlation with the wind-tunnel measurements is seen. Note that the CPU time of computing the AIC matrices of six reduced frequencies at one Mach number for the weakened wing is about 3.4 h on a 2.4-Ghz computer. Using the AIC matrices of the weakened wing, the flutter computation at four Mach numbers of the solid wing takes only 71 s.

Flutter Boundary of the Pitch-and-Plunge-Apparatus Wing

The pitch-and-plunge-apparatus (PAPA) wing has a camber supercritical airfoil with maximum thickness of 12% and a rectangular planform with chord of 0.406 m and semispan of 0.813 m (Ref. 15). The wind-tunnel flutter test of the PAPA wing was performed in NASA Langley's Transonic Dynamic Tunnel. The structural support of the PAPA wing provides only two modes: a plunge mode (3.43 Hz) and a pitch mode (5.44 Hz). Because of the simple structural

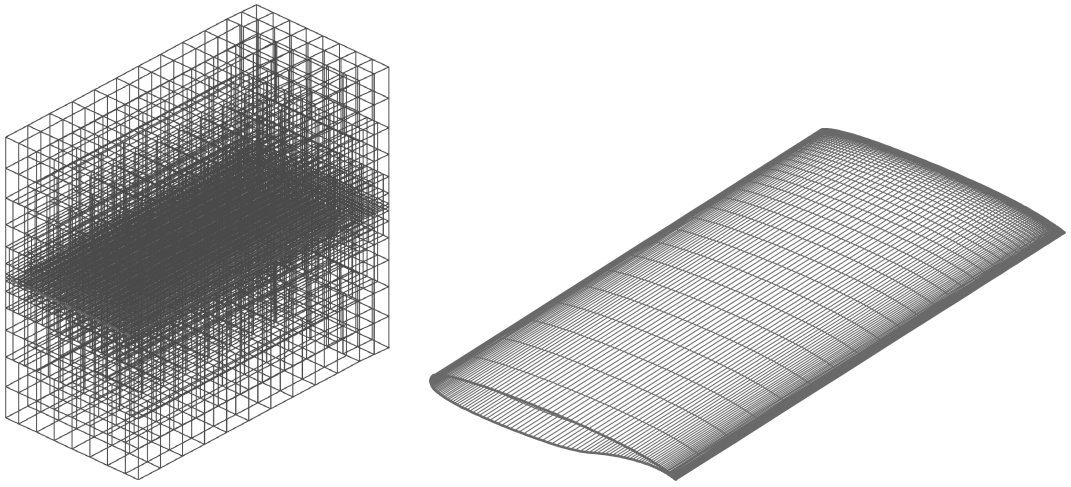

a) Field-panel model b) CFL3d surface mesh

Fig. 21 Field-panel model and CFL3D surface mesh of the PAPA wing.

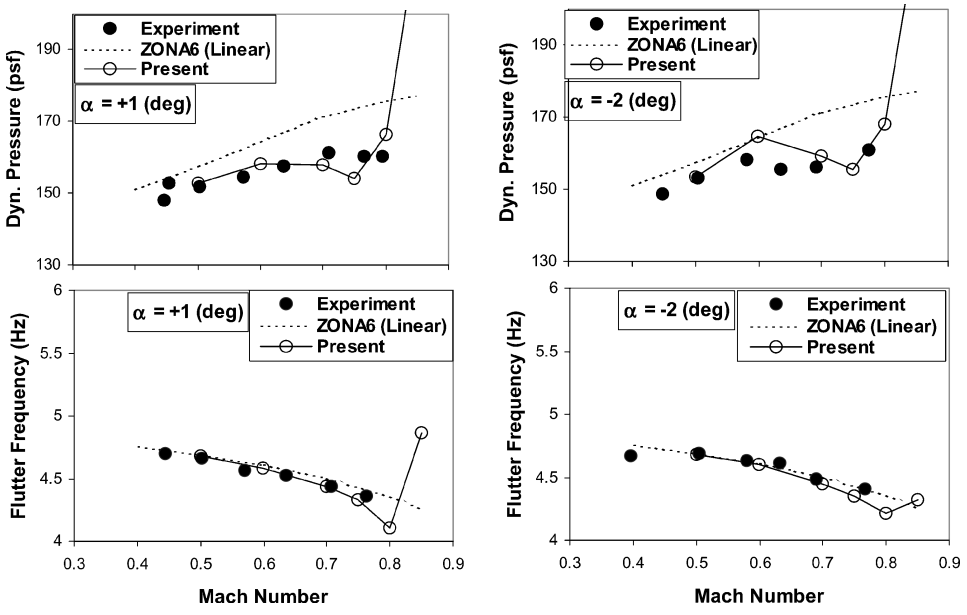

a) $\alpha = 1$ deg b) $\alpha = -2$ deg

Fig. 22 Flutter boundaries of the PAPA wing at $\alpha = 1$ and -2 deg.

arrangement and the complex aerodynamics caused by the supercritical wing characteristics, the objective of the wind-tunnel test was to provide experimental data for the validation of aeroelastic CFD codes. However, it turns out that only a few CFD results of the PAPA wing could be found in the open literature. This might be caused by the low-aerodynamic-damping characteristics of the PAPA wing, which requires a very long computational time to determine the accurate flutter boundary using the time-marching procedure of the CFD codes for transonic flutter predictions (Edwards, J. W., private communication, NASA Langley Research Center, Hampton, Virginia). However, this low-aerodynamic-damping characteristic is not a technical issue for the present method for flutter predictions because it is formulated in the frequency domain, whose unsteady aerodynamics can be directly adopted by a frequency-domain flutter solution procedure such as the g-method.[16]

Figure 21 presents a field-panel model and a CFL3D surface mesh of the PAPA wing. The steady background flows are provided by the CFL3D Navier–Stokes solver at Mach numbers ranging from 0.5 to 0.85, at $\alpha = 1$ and -2 deg, and at $Re = 1.25 \times 10^5$. The CFL3D results show that at $\alpha = 1$ deg the transonic shock starts appearing on the upper surface at $M_\infty = 0.7$ and moves to approximately 40% chord at $M_\infty = 0.8$. At $\alpha = -2$ deg, the transonic shock appears on the lower surface at $M_\infty = 0.7$ and moves to 40% chord at $M_\infty = 0.8$. These CFL3D results indicate the strong transonic effects on the PAPA wing as a result of its supercritical wing characteristic and present a challenge to the accuracy of the flutter predictions.

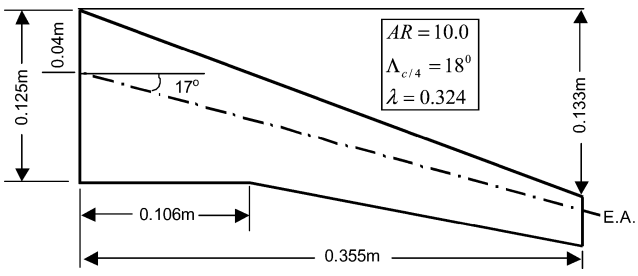

Fig. 23 Geometry of the YXX wing.

The flutter boundaries at $\alpha = 1$ and -2 deg obtained by the present method, the wind-tunnel test, and the linear method (ZONA6), are presented in Fig. 22. It can be seen that the transonic flutter dips are well predicted by the present method, verifying that the present method can deal with the strong shock cases on the supercritical

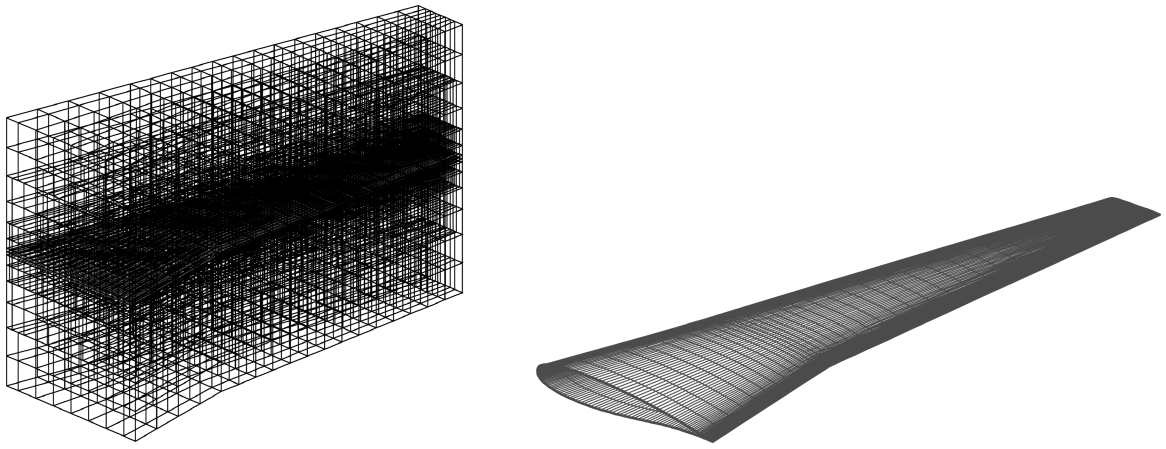

a) Field-panel model b) CFL3D surface mesh

Fig. 24 Field-panel model of CFL3D surface mesh of the YXX wing.

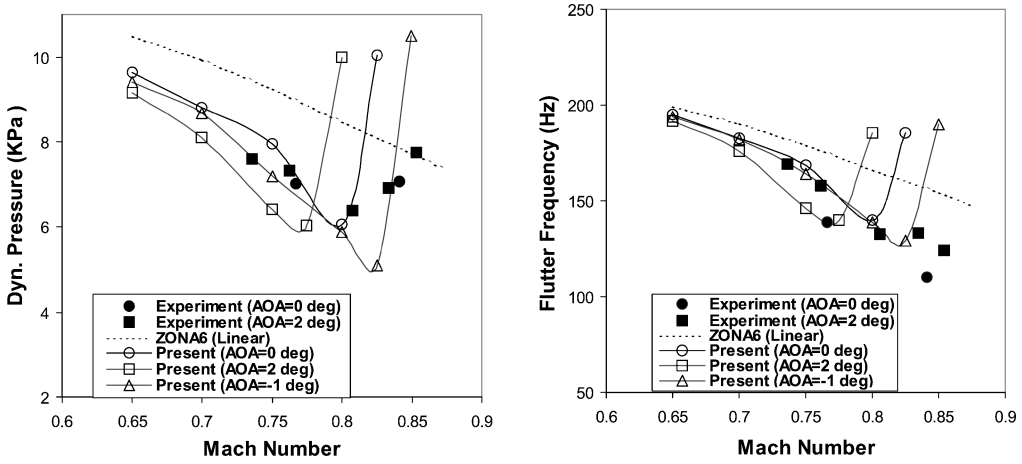

Fig. 25 Flutter boundaries of the YXX wing.

wings provided that steady background flow is accurately predicted by the high-fidelity CFD code such as CFL3D. Results also show that the flutter boundary of the PAPA wing in the transonic region is angle-of-attack dependent. Clearly, this angle-of-attack effect on flutter boundary cannot be accounted for by the linear methods such as ZONA6. The CPU time of the present method for this case is approximately 3 h per Mach number on a 2.4-Ghz computer.

Flutter Boundary of the YXX Wing

Figure 23 depicts the geometric description of the YXX wing that has an aspect ratio of 10.0, a 17-deg quarter-chord swept angle, and supercritical airfoil sections tapered from 16% thick at the root to 12% at the tip. The flutter boundary of the YXX wing was measured by Yonemoto[17] and computed by Isogai[18] using a full potential code with a two-dimensional boundary-layer correction. The flutter boundary of the YXX wing is extremely sensitive to the location of the center of pressure; according to Isogai, a 2% shift in the elastic axis causes a 70% shift in the flutter dynamic pressure at $M_\infty = 0.7$ (Ref. 19). In addition, the YXX wing has a large static aeroelastic deformation even at low angle of attack. Based on Isogai's computational results, the tip of the YXX wing can have a 4.4-deg nose-down angle and a -0.002-m vertical displacement at $M_\infty = 0.8, \alpha = 1$ deg, and dynamic pressure $= 61.54$ kPa. Of course, if such a large static aeroelastic deformation occurs, it can significantly alter the location of the center of pressure, indicating the strong dependence of the YXX wing flutter boundary on its static aeroelastic deformation.

Figure 24 depicts the field-panel model and the CFL3D surface mesh of the YXX wing. The CFL3D Navier–Stokes computations are performed at Mach numbers ranging from 0.654 to 0.85, at $\alpha = -1$, 0, and 2 deg, and at $Re = 2.4 \times 10^6$ to provide the steady background flows to the present method. Note that these CFL3D results are obtained on the "rigid" YXX wing geometry; no static aeroelastic deformation is included.

The flutter boundary predicted by the present method at $\alpha = -1$, 0, and 2 deg along with the wind-tunnel measured data and the ZONA6 computed results are presented in Fig. 25. The results of the present method show that angles of attack have a strong impact on the YXX wing flutter boundary in transonic flows, and among all angle-of-attack cases the predicted flutter boundary by the present method at $\alpha = -1$ deg correlates the best with the experimental data. The discrepancy between the present results and the experimental data is believed caused by the exclusion of the static aeroelastic deformation in the CFL3D mesh. Therefore, the validation of the present method on the YXX wing is presently inconclusive because of the lack of the static aeroelastic effects in the steady background flow. However, the best correlation at $\alpha = -1$ deg does indicate the correct trend of the present results because, among the $\alpha = 2$, 0, and -1 deg cases, the steady background flow at $\alpha = -1$ deg computed by CFL3D should be the closest one to that of a static aeroelastic deformed YXX wing with a 4-deg nose-down angle at the tip. Nevertheless, to conclude this YXX wing validation case, it requires further studies using a static aeroelastic CFD procedure to accurately determine the steady background flow with static aeroelastic effects.

Conclusions

An overset field-panel method has been developed for the transonic aerodynamic influence coefficient (AIC) matrix generation

and aeroelastic applications. The present method can be considered as a transonic counterpart of ZONA6/doublet-lattice method (DLM) because the surface boxes of the field-panel model can adopt those of ZONA6 or DLM. To generate the volume cells on lifting surfaces or bodies requires only a few additional input parameters such as the height and number of layers of the volume block. The overset field-panel scheme can minimize the volume-cell generation efforts on complex configurations and automatically transmit the interference between overset blocks. In addition, a block-tridiagonal approximation technique is incorporated in the present method to greatly improve the computational efficiency of solving the volume-cell influence coefficient matrix, which is a complex, fully populated, and normally very large size matrix.

The transonic AIC matrix generated by the present method has the same form as that of the linear panel methods and can be readily plugged into any existing AIC-based aeroelastic design processes for rapid flutter, aeroservoelastic, and dynamic loads analyses. To generate an AIC matrix for a lifting surface configuration at one reduced frequency takes about a half an hour of CPU time, but once generated it can be repeatedly used in a structural design loop, rendering the present method as an ideal tool for the multidisciplinary optimizations.

The present method also shows that simple theories based on the small disturbance approach can yield accurate unsteady transonic flow predictions if accurate steady background flow is given. This is demonstrated by the good correlation with the experimental data of the present results using the high-fidelity CFL3D Navier–Stokes solutions on the F-5 wing, the Lessing wing, the LANN wing, the AGARD 445.6 wing, the pitch-and-plunge-apparatus wing, and the YXX wing.

Acknowledgments

The authors thank Shuquan Lu of Nanjing Aeronautical Institute for his introduction of the transonic doublet-lattice method. Also, the authors thank Koji Isogai for providing the structural data of the YXX wing.

References

[1]Rodden, W. P., Giesing, J. P., and Kalam, T. P., "New Method for Nonplanar Configurations," AGARD, CP-80-71, Pt. 2, No. 4, 1971.

[2]Chen, P. C., Lee, H. W., and Liu, D. D., "Unsteady Subsonic Aerodynamics for Bodies and Wings with External Stores Including Wake Effort," *Journal of Aircraft*, Vol. 30, No. 5, 1993, pp. 618–628.

[3]Chen, P. C., and Liu, D. D., "Unsteady Supersonic Computation of Arbitrary Wing–Body Configurations Including External Stores," *Journal of Aircraft*, Vol. 27, No. 2, 1990, pp. 108–116.

[4]Voss, R., "Calculation of 3D Unsteady Transonic Potential Flows by a Field Panel Method," *2nd International Symposium on Aeroelasticity and Structural Dynamics*, Aachen, Germany, 1985, pp. 33–46.

[5]Lu, S., and Voss, R., "TDLM-A Transonic Doublet Lattice Method for 3D Potential Unsteady Transonic Flow Computation," DLR Institut fur Aeroelastik, DLR-FB 92-25, Goettingen, Germany, Sept. 1992.

[6]Tseng, K., and Merino, L., "Nonlinear Green's Function Method for Unsteady Transonic Flows," *Transonic Aerodynamics*, edited by D. Nixon, Vol. 81, Progress in Astronautics and Aeronautics, AIAA, New York, 1982, pp. 565–603.

[7]Murman, E. M., "Analysis of Embedded Shock Waves Calculated by Relaxation Methods," *AIAA Journal*, Vol. 12, No. 5, 1974, pp. 626–633.

[8]Van Zyl, L. H., "A Transonic Doublet Lattice Method for General Configurations," *International Forum on Aeroelasticity and Structural Dynamics*, Rome, 1997, pp. 25–31.

[9]Liu, D. D., Kao, Y. F., and Fung, K. Y., "An Efficient Method for Computing Unsteady Transonic Aerodynamics of Swept Wings with Control Surfaces," *Journal of Aircraft*, Vol. 25, No. 1, 1998, pp. 25–31.

[10]Krist, S. L., Biedron, R. T., and Rumsey, C. L., "CFL3D User's Manual," NASA Langley Research Center, Hampton, VA, Sept. 1997.

[11]Tijdeman, H., and Nunen, J. W. G. v., "Transonic Wind-Tunnel Tests on an Oscillating Wing with External Stores," AFFDL-TR-78-189, Pt. 2, Sept. 1978.

[12]Lessing, H. C., Troutman, J. L., and Menees, G. P., "Experimental Determination on a Rectangular Wing Oscillating in the First Bending Mode for Mach Numbers from 0.24 to 1.30," NASA TND-33, Dec. 1960.

[13]Malone, J. B., and Ruo, S. Y., "LANN Wing Test Program: Acquisition and Application of Unsteady Transonic Data for Evaluation of Three-Dimensional Computational Methods," AFWAL-TR-83-6006, Feb. 1983.

[14]Yates, E. C., "AGARD Standard Aeroelastic Configurations for Dynamic Response I-Wing 445.6," NASA TM 100492, Aug. 1987.

[15]Farmer, M. G., and Rivera, J. A., "Experimental Flutter Results of a Cambered Supercritical Wing on a Pitch and Plunge Apparatus," Aerospace Flutter and Dynamics Council Meeting, NASA Langley Research Center, Hampton, VA, May 1988.

[16]Chen, P. C., "Damping Perturbation Method for Flutter Solution: The g-Method," *AIAA Journal*, Vol. 38, No. 9, 2000, pp. 1519–1524.

[17]Yonemoto, Koichi, "A Practical Method for Predicting Transonic Wing Flutter Phenomena," International Council of the Aeronautical Sciences, Paper 84-1.7.1, Toulouse, France, Sept. 1984.

[18]Isogai, K., "Numerical Simulation of Transonic Flutter of a High-Aspect-Ratio Transport Wing," National Aerospace Lab., Rept. TR-776T, Japan, Aug. 1983.

[19]Shieh, T. H., Schoen, J. G., and Fung, K. Y., "Technique for Accurate, Efficient Computational of Unsteady Transonic Flow," AIAA Paper 91-0597, Jan. 1991.

E. Livne
Associate Editor